ISSN 0023-1584, Kinetics and Catalysis, 2011, Vol. 52, No. 1, pp. 119–127. © Pleiades Publishing, Ltd., 2011.

High Activities of Iron-FSM-16 Materials Synthesized by a Microwave-Hydrothermal Process in Friedel–Crafts Alkylations[1]

K. Bachari[a], R. M. Guerroudj[a], and M. Lamouchi[b]

[a]*Centre de Recherche Scientifique et Technique en Analysesphysico-Chimiques (C.R.AP.C.) BP 248, Alger RP 16004, Alger, Algérie*

[b]*Laboratoire de Catalyse et Environnement, EA 2598, MREI, Université du Littoral-Cote d'Opale, 145, Avenue Maurice Schumann, 59140 Dunkerque Cedex, France*

e-mail: bachari2000@yahoo.fr

Received November 1, 2009

Abstract—Iron-FSM-16 materials with different Si/Fe ratios (Si/Fe = 90, 60, and 10) have been synthesized by microwave-hydrothermal process and characterized by several spectroscopic techniques. X-ray diffraction, electron spin resonance, diffuse reflectance UV–visual and Mössbauer absorption spectroscopies allowed differentiation of several iron species. These species correspond to hematite particles, very small isolated Fe (III) species possibly incorporated in the mesoporous silica wall, and iron oxide clusters either isolated or agglomerated, forming "rafts" at the surface of the silica and exhibiting ferromagnetic ordering. Very importantly, catalytic data in benzylation of aromatic compounds such as benzene, toluene, and ethylbenzene with benzyl chloride shows that Fe-FSM-16 synthesized by microwave-hydrothermal process samples are very active and recycle catalysts.

DOI: 10.1134/S0023158411010034

Folded sheet mesoporous materials (FSM-16), which are analogous to the most extensively studied MCM-41 (Mobile Crystalline Material) (hexagonal, *p*6*mm*) materials, have gained much attention because of their high surface areas and pore volumes [1–4]. They possess a hexagonal array of channels with narrow pore size distributions. The formation mechanisms of the MCM-41 and FSM-16 materials have been studied in detail by Chen et al. [5]. The formation of MCM-41 materials is best explained by a liquid crystal templating mechanism [6]. On the other hand, FSM-16 materials are formed via a folded sheet mechanism in which the condensation of the reactive silanol groups present on the adjacent silicate layers in CTMA–kanemite complex leads to the formation of a hexagonal array of channels with uniform pore size [2], This mechanism is further substantiated by in situ energy dispersive X-ray diffraction measurements [7]. It is noteworthy that in comparison to MCM-41 materials, FSM-16 materials exhibit improved thermal stability, which is one of the key requirements for potential catalytic applications. This observed thermal stability can be attributed to their thicker pore walls [8–10]. Like MCM-41 materials, FSM-16 materials have widely been used as hosts to immobilize enzymes [11] and metal complexes [12–15]. Photofunctional $[Ru(bpy)_3]Cl_2$/FSM-16 materials are currently under increased investigation for the high potential they offer in the photooxidation of benzene to phenol [16]. It has been reported that fullerenes grafted FSM-16 materials are active catalysts for the liquid phase photooxidation of cyclohexene [17]. FSM-16 materials are also known to be effective catalysts for reactions such as photometathesis of propene [18, 19] and Beckmann rearrangement of cyclohexanone oxime to ε-caprolactam [20]. Recently, the preparations of Pt and Rh nanowires or nanoparticles in FSM-16 have also been reported [21, 22]. Furthermore, the microwave-hydrothermal synthesis of molecular sieves is a relatively new area of research [23–29]. It offers many distinct advantages over the conventional hydrothermal synthesis. They include rapid heating to crystallization temperature due to volumetric heating, resulting in homogeneous nucleation, fast super-saturation by the rapid dissolution of precipitated gels and eventually a shorter crystallization time compared to conventional autoclave heating [23–29]. It is also energy efficient and economical [23–29]. This method has been successfully applied for the syntheses of several types of zeolites namely zeolite A, Y, ZSM-5, MCM-41, metal substituted aluminophosphate, silico-aluminophosphate and gallophosphate [23–29]. It has also been successfully applied for the synthesis of mesostructured thiogermanates or germanium sulfides [30]. A rapid synthesis of titanium substituted MCM-41 molecular sieve has also been reported using micro-

[1] The article is published in the original.

wave-assisted approach [31]. Recently, a rapid synthesis of SBA-15 and Ti- and Zr-SBA-15 framework under microwave-hydrothermal conditions has been reported [32, 33].

Friedel–Crafts alkylations constitute a very important class of reactions, which are of common use in organic chemistry. Among these reactions, the liquid-phase benzylation of benzene and other aromatic compounds such as benzyl chloride and benzyl alcohol is important for the production of diphenylmethane (DPM) and substituted diphenylmethanes, which are important industrially as intermediates for pharmaceuticals and fine chemicals [34]. Fe-containing mesoporous materials have been proved effective heterogeneous solid catalysts for benzylation of benzene in previous reports [35–39]. Indeed, in the present study we report the synthesis and characterization of Fe-FSM-16 mesoporous molecular sieves synthesized by a microwave hydrothermal (M-H) process with different Si/Fe ratios (Si/Fe = 90, 60, and 10) and their test as catalysts for the liquid phase benzylation of benzene with benzyl chloride. These materials were characterized by N_2 adsorption measurements, X-ray diffraction (XRD), electron spin resonance (ESR), diffuse reflectance UV-visible (DR UV-vis), and Mössbauer absorption spectroscopies.

EXPERIMENTAL

Synthesis of the Catalysts

Microwave-hydrothermal synthesis of Fe-FSM-16 mesoporous molecular sieves with different Si/Fe ratios was performed using a MARS5 (CEM Corp., Matthews, NC, USA) microwave digestion system. This system operates at a maximum power of 1200 W and the power can be varied from 0 to 100% and is controlled by both pressure and temperature to a maximum of 350 psi and 513 K, respectively. A 2.45 GHz microwave frequency was used which is the same as that in domestic microwave ovens. The syntheses were carried out in double-walled digestion vessels which have an inner liner and cover made up of Teflon PFA and an outer strength vessel shell of Ultem polyetherimide. In a typical procedure kanemite (2.2 g) was added into a beaker containing a mixture of CTMABr (Cetyltrimethylammonium bromide) (0.79 g) and 38.0 ml of deionized water and stirred for 45 min. And then iron nitrate Fe $(NO_3)_3 \cdot 9H_2O$ (0.23 g) was added dropwise into the above mixture. This mixture was stirred for another 45 min. The pH of the final mixture was 11.8. The gel thus obtained was subjected to microwave-hydrothermal conditions for crystallization under static conditions at 373 K for 2 h. The crystallized product was filtered, washed thoroughly with deionized water, dried at 333 K and then calcined at 973 K in air for 12 h. In the other hand, as the iron content of the Fe-FMS-16 (Si/Fe = 60) solid was too low to allow the recording of Mössbauer spectra in suitable conditions, the compound was synthesized using Fe nitrate enriched with ^{57}Fe.

Characterization Techniques

The chemical compositions of the samples were determined by atomic absorption. Adsorption-desorption study of nitrogen was performed on a Micromeritics ASAP2010M volumetric adsorption analyzer at 77 K. A sample was degassed in vacuum at 573 K for 12 h before measurement. The surface area was calculated based on the BET (Brunauer–Emmett–Teller) method, while pore size distribution was computed using the BJH (Barrett–Joyner–Halenda) method. DR UV–vis spectra were collected on a Perkin-Elmer Lambda 9 spectrometer. XRD patterns obtained using a Siemens D500 diffractometer and CuK_α radiation, were recorded with 0.02° (2θ) steps and 1 s counting time per step between 1° and 10° (2θ) and between 10° and 80° (2θ). ESR spectra were recorded in the X band mode on a Varian E9 spectrometer at 77 and 295 K. The ESR data were fed directly into a PC for processing. Quantitative analyses of the relative populations of the identified Fe species were performed. Spectra of several solids were recorded after treatment overnight under vacuum at 445 K. DPPH (3314 G, $g = 2.0036$) was used as a standard for g-value determinations. The ^{57}Fe Mössbauer spectra of the samples were recorded between 298 and 4.2 K using a 2-GBq ^{57}Co/Rh source and a conventional constant acceleration spectrometer, operated in triangular mode. Spectra at temperatures below 4.2 K were obtained in a ^{3}He–^{4}He dilution refrigerator and in-field spectra with a superconducting coil. The applied magnetic field (H) was parallel to the γ-ray direction of propagation. The isomer shifts (δ) are given with respect to α-Fe at 293 K and calculated as the quadrupolar splittings (Δ) with a precision of about 0.02 mm/s. The validity of the computed fits was evaluated on the basis of both χ^2 values and convergence of the fitting process. The relative areas of the observed components were used to quantitatively evaluate the relative amounts of the iron species present in the catalysts, assuming equal recoil-free fractions for all catalysts.

Catalytic Testing

The liquid phase benzylation of benzene with benzyl chloride (BC) was carried out in a 50 ml three-necked round-bottomed flask equipped with a reflux condenser and heated in a precisely controlled oil bath under atmospheric pressure. In a typical run, 50 mg of catalyst, 6 ml of benzene, and 1 mmol of dodecane (internal standard) were added into the flask, followed by stirring for 30 min at required temperature (343 K). Then, 0.5 ml of BC was finally added. Samples were analyzed periodically on a gas chromatograph (HP-6890) equipped with a flame ionization detector and a

Table 1. Chemical composition and characteristics of the samples Fe-FSM-16 prepared by microwave-hydrothermal synthesis

Chemical analysis[a]		S_{BET}^{b}, $m^2 g^{-1}$	Pore volume[c], $cm^3 g^{-1}$	Pore diameter[d], Å	Wall thickness[e], Å
Si/Fe (gel)	Si/Fe				
90	88.5	820	0.89	22.0	20.2
60	59.2	788	0.81	24.5	19.8
10	9.6	700	0.75	22.3	19.5

[a] Iron content data from ICP-AES.
[b] Surface area calculated from BET equation.
[c] Pore volume calculated from the adsorption branch of the isotherm at $P/P_0 \approx 0.98$.
[d] Pore diameter calculated from the desorption branch of the isotherm according to BJH method.
[e] Wall thickness equals d-spacing (calcined sample) minus pore diameter (BJH).

capillary column RTX-1 (30 m × 0.32 mm i.d.). The products were also identified by GC-MS (HP-5973) analysis.

RESULTS AND DISCUSSION

XRD, N_2 Adsorption Isotherms, DR UV–vis Spectroscopy and Chemical Analysis

The Si/Fe ratios of the compounds were varied over a very wide range to characterize all of the iron species that may be formed in this type of compound. The elemental analyses of the synthesized compounds, presented in Table 1, correspond well to the nominal values. The BET surface areas and pore volumes of the Fe-FSM-16 samples are in the range of 700–820 $mm^2 g^{-1}$ and 0.75–0.89 $cm^3 g^{-1}$, respectively (Table 1). In the present case, the surface areas and pore volumes of the Fe-FSM-16 samples are lower than the values reported for FSM-16 materials prepared by conventional hydrothermal synthesis. The maximum values of the BET surfaces of the FSM-16 materials prepared by conventional hydrothermal synthesis are reported to be nearly in the range of 1070–1100 $m^2 g^{-1}$ [2]. One possible explanation for the lower surface areas and pore volumes is that the pore walls of the Fe-FSM-16 samples prepared by M-H synthesis are thicker than the FSM-16 samples prepared by conventional hydrothermal synthesis reported in the literature [3, 4]. The X-ray powder diffraction patterns of the solids prepared by M-H synthesis showed 3 peaks indexed as (100), (110), and (200) reflections in the range of $2\theta = 2°–5°$, which are corresponding to the well-ordered hexagonal mesoporous structure (Fig. 1). The intensity of these peaks decreased when the iron content increased showing that the addition of iron has a negative effect on the crystallinity. At the same time, small peaks corresponding to α-Fe_2O_3 (hematite form) appeared in the 10° to 80° (2θ) range and grew with the iron content (Fig. 2). The DR UV–vis spectra of the samples Fe-FSM-16 (Si/Fe = 90, 60, and 10) showed one absorption band at 230–280 nm, corresponding to oxygen-to-metal charge transfers involving isolated tetrahedrally coordinated ferric cations (Fig. 3). When the iron content of the solids increases, a broad band appears with a maximum around 350 nm. The presence of this band, which is characteristic of iron oxide, is in good agreement with the XRD data.

^{57}Fe Mössbauer Spectroscopy

The spectra of the as-prepared compounds recorded at 295 K show the same ferric doublet, with an isomer shift $\delta = 0.33 \pm 0.02$ mm/s and a quadrupolar splitting $\Delta = 0.86 \pm 0.02$ mm/s. Along with the doublet, the richer iron catalyst Fe-FSM-16 (Si/Fe = 10) exhibits a magnetic sextet. This sextet, with a quadrupolar splitting of $\Delta = -0.22$ mm/s and a hyperfine field of 52.0 T, can be assigned without ambiguity to hematite α-Fe_2O_3 [40]; this correlates well with the XRD analysis of the sample showing the presence of such a phase. To evaluate the doublet observed at room tem-

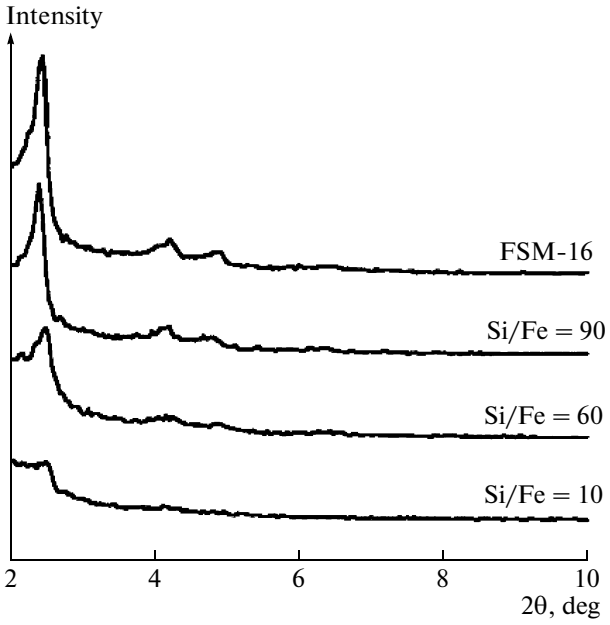

Fig. 1. XRD patterns of Fe-FSM-16 materials in the domain of 1°–10° (2θ).

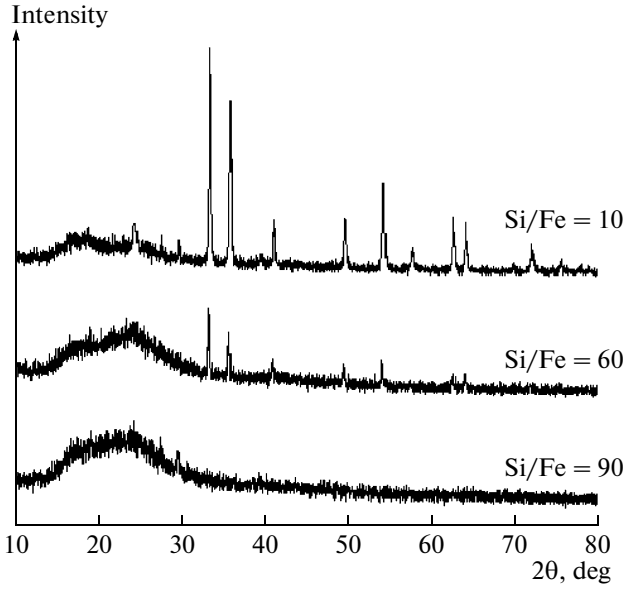

Fig. 2. XRD patterns of the Fe-FSM-16 materials in the domain of 10°–80° (2θ).

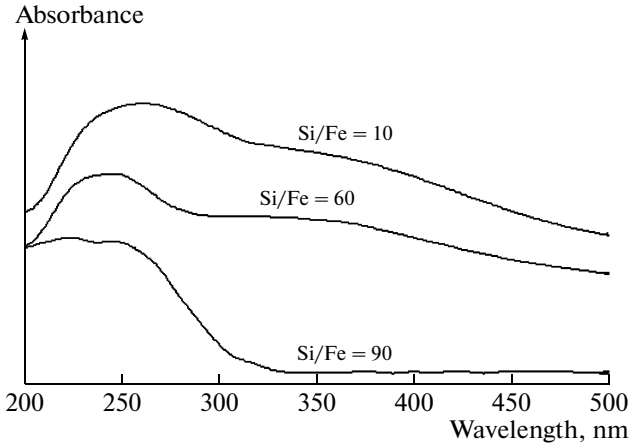

Fig. 3. DR UV–vis spectra of the Fe-FSM-16.

perature, we recorder spectra at lower temperatures. The spectra obtained for Fe-FSM-16 (Si/Fe = 60) at temperatures between 77 and 4.2 K are presented in Fig. 4. Indeed, initially the Fe-FSM-16 (Si/Fe = 60) material shows two components: a quadrupolar doublet, visible even at 4.2 K, and a magnetic sextet with rather broad lines. However, at intermediate temperatures (40 K), another weak intensity (6%) magnetic sextet is visible, with a large hyperfine field of 54 T and rather narrow lines. At 77 K only this sextet is present with a quadrupolar doublet. The isomer shifts of these components are similar: $\delta = 0.48$ mm/s, typical for ferric compounds at low temperature. At this stage we can identify two Fe species in the spectra: hematite (α-Fe_2O_3), corresponding to the 6% sextet with hyperfine field of 54 T, and a super-paramagnetic oxide-like species [41], giving rise to the doublet and main sextet. As temperature increases, the growing of the intensity of the doublet at the expense of the sextet is a behavioral characteristic of nanosized magnetic particles, due to the increasing number of particles with rapidly fluctuating, magnetization, that is, with a time scale shorter than the hyperfine Larmor time $\tau_L \cong 10^{-8}$ s associated with ^{57}Fe [42]. The magnetization of a particle with volume V fluctuates according to an Arrhenius law, $1/\tau = 1/\tau_0 \exp(-U/k_BT)$, where $\tau_0 \cong 10^{-10}$–10^{-11} s is a microscopic trial time and $U = KV$ is the anisotropy barrier, K being the density of anisotropy energy ($K \cong 10^4$–10^5 erg/cm^3) characteristic of the material. The "blocking volume" $V_b(T)$ at temperature T for ^{57}Fe Mössbauer spectroscopy is such that $1/\tau = 1/\tau_L$; it is given by the expression $V_b(T) = k_BT/K\ln(\tau_L/\tau_0)$, and it is an increasing function of T. Thus, as temperature increases, more and more particles have $V < V_b$, implying $1/\tau > 1/\tau_L$ and show a spectrum in which the magnetic hyperfine interaction has been smeared out, leaving the quadrupolar doublet alone. In Fig. 4 the magnetic hyperfine sextet with broad lines has been accounted for by a distribution (histogram) of hyperfine fields with a peak value decreasing from 50 T at 4.2 K to around 35 T at 40 K. The splitting of the quadrupolar doublet is $\Delta = 0.94(2)$ mm/s in this low-temperature range. To check whether a quadrupolar doublet is still present below 4.2 K, a study of the Fe-FSM-16 (Si/Fe = 60) sample was conducted at low temperature. Spectra were recorded at 1 and 0.05 K (Fig. 5). At 0.05 K a sizeable quadrupolar doublet (12%) is seen, but with hyperfine parameters [$\delta = 0.53(2)$ mm/s and $\Delta = 1.15(3)$ mm/s] slightly different than those of the super-paramagnetic doublet observed at higher temperature. The persistence of a doublet down to temperatures as low as 0.05 K already has been observed for several iron oxide-supported catalysts [43, 44]. For small magnetic particles, fluctuations of magnetization are "frozen" below 1 K with respect to the Larmor time τ_L. Thus, the presence of the doublet demonstrates rapid magnetic relaxation at very low temperature and can be related either to "isolated" ferric iron, for which only long-range dipolar interaction exists, or to ferric cations forming small oligomers, also allowing rapid exchange-driven spin fluctuations. Therefore, the Fe-FSM-16 (Si/Fe = 60) sample prepared by M-H synthesis has the following composition (in Fe at %): 12% in small oligomers, 5% in hematite, and 83% in an oxide-like super-paramagnetic species. To further characterize this latter species, Fig. 6 plots the thermal variation of the fraction of its quadrupolar doublet. It rises rapidly up to 4 K, then more slowly, with an S-like shape, up to 80 K, at which point it reaches 100%. This two-stage evolution points to the existence of a bimodal size distribution for the super-paramagnetic particles. The inset in Fig. 6 shows the size distribution required to reproduce the experimental thermal variation of the doublet fraction, assuming a density of anisotropy energy of

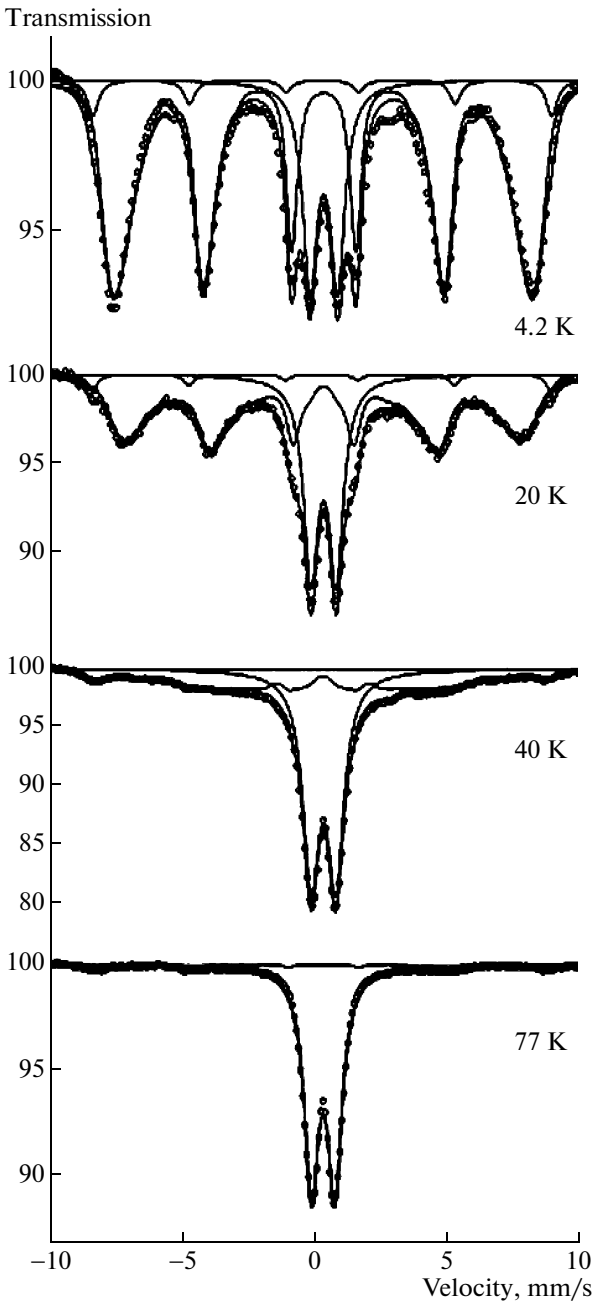

Fig. 4. ^{57}Fe Mössbauer absorption spectra of the Fe-FSM-16 (Si/Fe = 60) material at different temperatures.

$K = 4 \times 10^4$ erg/cm^3. The super-paramagnetic fraction is calculated as:

$$f_P(T) = \frac{1}{\langle V \rangle} \int_{V_{min}}^{V_b} V f(V) \mathrm{d}V.$$

where $f(V)$ is the size distribution function. The solid line in Fig. 6 is the calculated curve; above about 5 K all of the smaller particles (mean diameter 2 nm) are super-paramagnetic, and the larger particles (mean diameter 9 nm) reach the super-paramagnetic regime

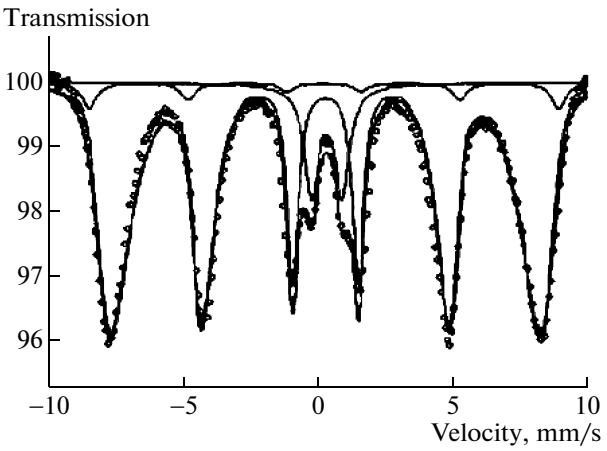

Fig. 5. ^{57}Fe Mössbauer absorption spectrum of the Fe-FSM-16 (Si/Fe = 60) material at 0.05 K.

at 80 K. To obtain clues about the magnetic structure of the observed Fe species, spectra were recorded in the Fe-FSM-16 (Si/Fe = 60) sample at 4.2 K with applied magnetic fields of 2 and 7 T (Fig. 7). The recorded spectra show components similar to those distinguished at 4.2 K in zero fields: anti-ferromagnetic hematite, a doublet-like sub-spectrum, and a broad sextet. As the applied field increases, the intensity of the intermediate lines of the sextet strongly decreases. This shows that the hyperfine fields of the Fe (III) species progressively reorient toward the field. At the same time, the hyperfine field distribution center decreases from 50 T in zero field to 46 T at 7 T. This type of response to the field is typical of a ferromagnetic ordering; for Fe (III) the hyperfine field is antiparallel to the magnetic moment, which aligns along the applied field.

ESR Spectroscopy

ESR spectra of the compounds prepared by M-H synthesis were recorded at 77 K under N_2 (Fig. 8) and after dehydration under vacuum at 623 K (Fig. 9). Four signals at $g = 7.5$, 4.5, 2.5, and 2.0 can be distinguished. The signal at $g = 4.5$ is currently observed for iron oxide materials supported on various substrates and attributed to isolated octahedral or tetrahedral Fe (III) sites with a strong rhombic distortion [45, 46]. The smallest and broader signal at $g = 7.5$ was previously observed in the same type of solids but not assigned [47]. The signal at $g = 2.0$ often has been attributed to octahedrally coordinated Fe (III) cations; it has been proposed to generally correspond to extra-framework iron species observed in zeolitic material characterization and can be assigned to the super-paramagnetic iron oxide clusters [48–50]. The interpretation of the small signal at $g = 2.5$, which also is frequently detected in iron-supported catalysts or zeolites, is still matter of debate. It has been assigned

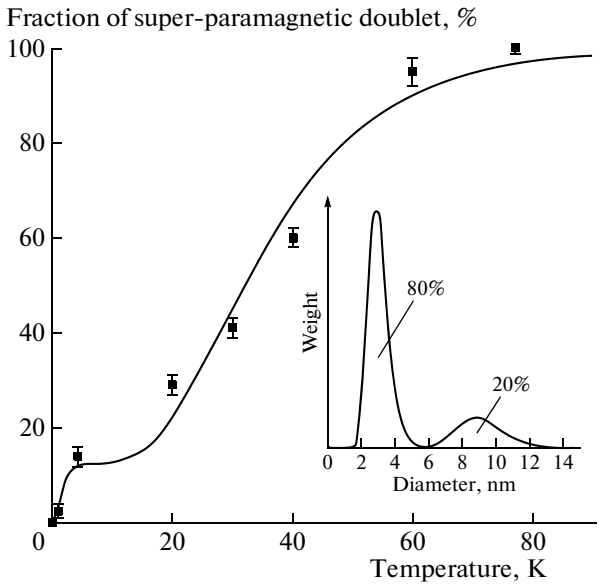

Fig. 6. Variation of the fraction of the super-paramagnetic doublet intensity as a function of temperature in the Fe-FSM-16 (Si/Fe = 60). (The solid line is a calculation using the particle size distribution shown in the inset and a value of the anisotropy constant $K = 4 \times 10^4$ erg/cm^3.)

either to small iron oxide aggregates or to 3-coordinated species in the framework of zeolitic materials [51]. The latter species is sensitive to adsorbed molecules like H_2O. When attributed to small aggregates, it generally disappears after heat treatment under a reducing atmosphere or vacuum because of the reduction of iron, whereas it increases when attributed to the second species due to desorption of adsorbed molecules. In the present study, the signal, which is very small, apparently increased after heat treatment under vacuum and may be attributed to 3-coordinated species; although a partial attribution to iron oxide aggregates cannot be excluded in view of the other characterization data. 3-Coordinated species are formed by either dehydroxylation or dehydration of 4-coordinated hydroxylated species. After dehydration under vacuum at 623 K, the main signal at $g = 2.0$ disappeared, whereas those at $g = 4.5$ and 2.5 were still present. The disappearance of the first signal may be related to the reduction of the very small "nanoparticles." Such reduction did not seem to affect the other species, which may be attributed to oligomeric iron species in more or less solid solution in the silicic mesoporous walls and corresponding to those giving a doublet in the Mössbauer spectra even at very low temperature (0.05 K). A new signal characterized by a $g = 6.1$ appears. Such a signal was previously observed with two other signals with $g = 4.3$–9.0 for FeS-1 outgassed at 673 K [52]. It was assigned to a distorted tetrahedron, which maintains an axial asymmetry. Finally, we observed that the transformation was totally reversible: treating the material for 24 h at room temperature in ambient air restored the original spectrum.

Friedel–Crafts Alkylations

Figure 10 shows the conversion of BC in benzylation of benzene with BC over Fe-FSM-16 catalysts prepared by M-H synthesis with various Si/Fe ratios, and catalytic selectivity and turnover frequency (TOF) are presented in Table 2. The products in this reaction are diphenylmethane and the isomers of dibenzylbenzene (DBB)—1,4-DBB, 1,3-DBB, and 1,2-DBB. Notably, all catalysts exhibit excellent catalytic activities, giving the complete conversion of BC in 25–65 min. Interestingly, the activities are strongly dependent on iron loading in the samples. For example, it

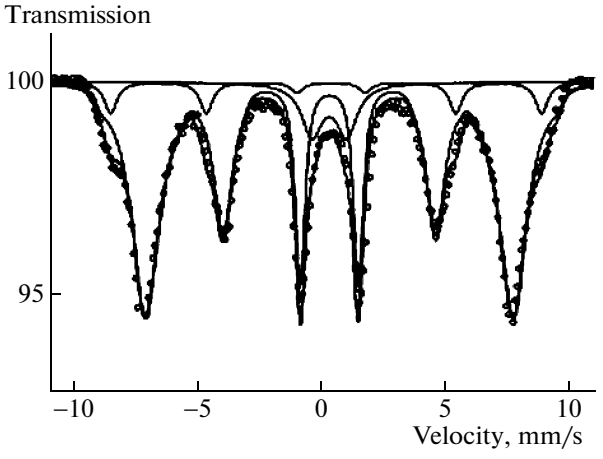

Fig. 7. ^{57}Fe Mössbauer absorption spectrum of the Fe-FSM-16 (Si/Fe = 60) at 4.2 K with a magnetic field of 7 T applied parallel to the γ-ray direction of propagation.

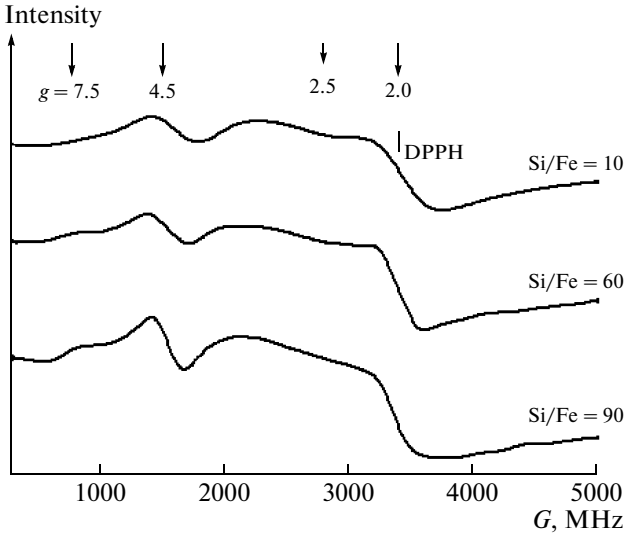

Fig. 8. ESR spectra of the Fe-FSM-16 recorded at 77 K.

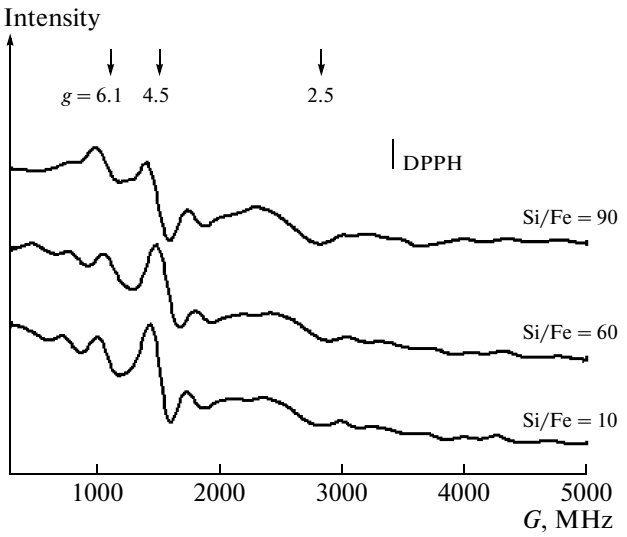

Fig. 9. ESR spectra of the Fe-FSM-16 recorded at 77 K after reduction at 623 K under vacuum.

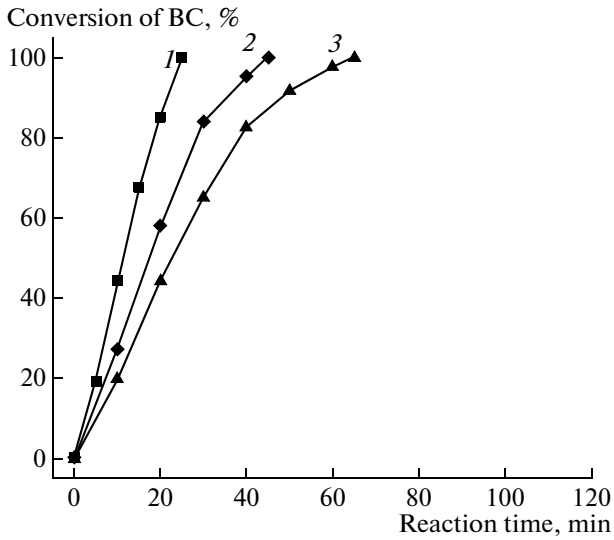

Fig. 10. Benzyl chloride conversion on reaction time at 343 K over Fe-FSM-16 catalysts with various Si/Fe ratios: *1*—10, *2*—60, *3*—90.

needs 65 min for near 100% conversion of benzyl chloride over Fe-FSM-16 (Si/Fe = 90), but it takes for 24 min over Fe-FSM-16 (Si/Fe = 10). Based on classical mechanism of Friedel–Crafts alkylations, one or more electron-donating groups in the aromatic ring will facilitate benzylation of an aromatic compound [34]. Unfortunately, as observed in Fe-SBA-15 [36] and Fe-HMS [37], catalytic activities are reduced by introduction of electron-donating groups in the aromatic compound, which are assigned to possible poisoning caused by the strong adsorption of the aromatic substrate [36]. Table 3 presents the conversion of BC and product selectivity in benzylation of aromatic compounds with various electron-donating groups such as methyl and methoxy over Fe-FSM-16 (Si/Fe = 60) at 343 K. For example, the complete conversion of BC with benzene takes 45 min, but the complete conversion of BC with toluene and anisole takes 20 and 15 min, respectively. These results indicate that electron-donating groups in the aromatic ring significantly facilitate benzylation over Fe-FSM-16 (Si/Fe = 60) sample. It is also interesting to note that the time for complete conversion of BC with xylenes and ethylbenzene is longer than that of BC with toluene. Obviously, this case cannot be solely explained by the electron-donating groups because electron-donating ability in xylenes and ethylbenzene is stronger than that in toluene. Possibly, in this case, steric effects may be another factor for the catalytic activity [53]. Additionally, when the conversion of BC reaches 100% in benzylation of toluene, the catalyst of Fe-FSM-16 (Si/Fe = 60) was separated from the solution completely, followed by the addition of another 0.5 ml of BC. Interestingly, there is negligible BC conversion after reaction for 60 min, indicating that there is no leaching of catalytic sites Fe-FSM-16 (Si/Fe = 60). Furthermore, after being separated from the solution, the catalyst of Fe-FSM-16 (Si/Fe = 60) was regenerated by calcination at 773 K for 2 h. The regenerated catalyst still shows high activity in benzylation of toluene with BC, even if twice recycles Fe-FSM-16 (Si/Fe = 60) still gives at near 100% BC conversion within 20 min. Apparently, Fe-FSM-16 solids is an active and recycled catalyst for benzylation of aromatic compounds with BC. In summary, we can propose a follow mechanism which involves oxidation of benzyl chloride on iron cations with formation of a charge transfer complex:

$$\varnothing\text{-}CH_2Cl + Fe^{3+} \rightleftharpoons \varnothing\text{-}CH_2Cl^{+\cdot} + Fe^{2+},$$

$$\varnothing\text{-}CH_2Cl^{+\cdot} \rightleftharpoons \varnothing\text{-}CH_2^{+} + Cl,$$

$$Fe^{2+} + Cl^{\cdot} \rightleftharpoons Fe^{3+} + Cl^{-}.$$

Indeed, with a Si/Fe ratio 60 iron atoms are present mainly as nanometric clusters. With increasing iron content (Si/Fe = 10), the large hematite particle content increases, whereas with decreasing iron content (Si/Fe = 90), the oligomer content is maximized. The

Table 2. Benzylation of benzene with benzyl chloride over various Fe-FSM-16 catalysts at 343 K. Reaction conditions: 6 mL of benzene, 0.5 ml of benzyl chloride, 50 mg of catalyst. The conversion was calculated from benzyl chloride

Si/Fe	Time[a], min	Selectivity[b], %	TOF[c], min^{-1}
90	65	100	7
60	45	100	8
10	24	98	10

[a] Time required for complete conversion of benzyl chloride.
[b] Selectivity for diphenylmethane.
[c] Moles of benzyl chloride converted per mole of Fe in the catalyst per min.

Table 3. Benzylation of substituted benzene with benzyl chloride over Fe-FSM-16 (Si/Fe = 60) catalyst at 343 K. Reaction conditions: 6 mL of benzene, 0.5 mL of benzyl chloride, 50 mg of catalyst. The conversion was calculated from benzyl chloride

Substituent	Time[a], min	Reaction products (selectivity, %)
Benzene	45	Diphenylmethane (100)
Toluene	20	*p*-4-Methyldiphenylmethane (58)
		o-2-Methyldiphenylmethane (42)
p-Xylene	30	2,5-Dimethyldiphenylmethane (100)
Anisole	15	*p*-4-Methoxydiphenylmethane (66)
		o-2-Methoxydiphenylmethane (34)
Mesitylene	10	2,4,6-Trimethyldiphenylmethane (100)
Toluene[b]	20	*p*-4-Methyldiphenylmethane (60)
		o-2-Methyldiphenylmethane (40)

[a] Time required for complete conversion of benzyl chloride.
[b] The data were obtained after twice recycles.

low reactivity of the catalysts with low iron content hypothetically may be attributed to the fact that iron cations that are almost isolated or in very small oligomers cannot be reduced under the reaction conditions. Indeed, it was interesting to compare the solids with Fer containing aluminophosphate molecular sieves prepared by conventional hydrothermal synthesis investigated earlier under similar conditions [54]. Both systems reached a final conversion of 100% with complete selectivity to monoalkyl; a time required for complete conversion of benzyl chloride was about 85.9 min for $FAPO_4$-5 prepared conventional hydrothermal synthesis and was here about 45 min, so that Fe-FSM-16 materials prepared by M-H synthesis is more active than Fe-containing aluminophosphate molecular sieves prepared by conventional hydrothermal synthesis.

The characterization by XRD, DR UV–vis, ESR, and Mössbauer spectroscopy of Fe-FSM-16 materials prepared by microwave-hydrothermal synthesis has shown that several iron species could be identified at the surface of the pore walls of the mesoporous silica, including very small Fe (III) isolated cations close to each other, remaining paramagnetic down to very low temperature (0.05 K); super-paramagnetic nanometric or sutenanometric small clusters undergoing a ferromagnetic type of ordering; and anti-ferromagnetic large hematite particles. In the materials with a Si/Fe ratio 60 iron atoms are present mainly as nanometric clusters. With increasing iron content (Si/Fe =10), the large hematite particle content increases, whereas with decreasing iron content (Si/Fe = 90) the oligomer content is maximized. Finally, our findings clearly demonstrate the great interest of recording Mössbauer spectra below 4.2 K. This provided evidence of the formation of nanometric iron clusters at the surface of the mesoporous silica. Standard low-temperature studies, as have been conducted in the vast majority of cases above 4.2 K, would have concluded to the presence of larger particles; the analysis by Mössbauer spectroscopy performed at lower temperature demonstrated that these particles were agglomerations of nanometric iron clusters. The spectroscopic technique performed below 4.2 K allowed us to reach another level of resolution of the ferric particle structures. More importantly, Fe-FSM-16 samples prepared by microwave-hydrothermal synthesis as solid catalysts are very active for liquidphase benzylation of aromatic compounds with BC.

REFERENCES

1. Yanagisawa, T., Shimizu, T., Kuroda, K., and Kato, C., *Bull. Chem. Soc. Jpn.*, 1990, vol. 63, p. 988.
2. Inagaki, S., Fukushima, Y., and Kuroda, K., *J. Chem. Soc., Chem. Commun.*, 1993, p. 680.
3. Kuroda, K., *J. Porous Mater.*, 1996, vol. 3, p. 107.
4. Sakamoto, Y., Inagaki, S., Ohsuna, T., Ohnishi, N., Fukushima, Y., Nozue, Y., and Terasaki, O., *Micropor. Mesopor. Mater.*, 1998, vol. 21, p. 589.
5. Chen, C.-Y., Xiao, S.-Q., and Davis, M.E., *Microporous Mater.*, 1995, vol. 4, p. 1.
6. Kresge, C.T., Leonowicz, M.E., Roth, W.J., Vartuli, J.C., and Beck, J.S., *Nature*, 1992, vol. 359, p. 710.
7. O'Brien, S., Francis, R.J., Fogg, A., O'Hare, D., Okazaki, N., and Kuroda, K., *Chem. Mater.*, 1999, vol. 11, p. 1822.
8. Li, W., Yao, Y., Wang, Z., Zhao, J., Zhao, M., and Sun, C., *Mater. Chem. Phys.*, 2001, vol. 70, p. 144.
9. Kimura, T., Itoh, D., Okazaki, N., Kaneda, M., Sakamoto, Y., Tereasaki, O., Sugahara, Y., and Kuroda, K., *Langmuir*, 2000, vol. 16, p. 7624.
10. Kimura, T., Kamata, T., Fuziwara, M., Takano, Y., Kaneda, M., Sakamoto, Y., Terasaki, O., Sugahara, Y., and Kuroda, K., *Angew. Chem., Int. Ed. Engl.*, 2000, vol. 39, p. 3855.
11. Takahashi, H., Li, B., Sasaki, T., Miyazaki, C., Kajino, T., and Inagaki, S., *Microporous Mesoporous Mater.*, 2001, vols. 44–45, p. 755.
12. Chen, H., Matsumoto, A., Nishimiya, N., and Tsutsumi, K., *Chem. Lett.*, 1999, p. 993.
13. Chen, H., Matsumoto, A., Nishimiya, N., Takeichi, T., and Tsutsumi, K., *Microporous Mesoporous Mater.*, 2000, vol. 40, p. 289.
14. Ogawa, M., Kuroda, K., and Nakamura, T., *Microporous Mesoporous Mater.*, 2001, vol. 48, p. 159.
15. Ogawa, M., Kuroda, K., and Nakamura, T., *Chem. Lett.*, 2002, p. 632.
16. Fujishima, K., Fukuoka, A., Yamagishi, A., Inagaki, S., Fukushima, Y., and Ichikawa, M., *J. Mol. Catal. A: Chem.*, 2001, vol. 166, p. 211.
17. Fukuoka, A., Fujishima, K., Chiba, M., Yamagishi, A., Inagaki, S., Fukushima, Y., and Ichikawa, M., *Catal. Lett.*, 2000, vol. 68, p. 241.

18. Yoshida, H., Kimura, K., Inaki, Y., and Hattori, T., *Chem. Commun.*, 1997, p. 129.
19. Inaki, Y., Yoshida, H., Kimura, K., Inagaki, S., Fukushima, Y., and Hattori, T., *Phys. Chem. Chem. Phys.*, 2000, vol. 2, p. 5293.
20. Shouro, D., Ohya, Y., Mishima, S., and Nakajima, T., *Appl. Catal., A*, 2001, vol. 214, p. 59.
21. Fukuoka, A., Higashimoto, N., Sakamoto, Y., Inagaki, S., Fukushima, Y., and Ichikawa, M., *Microporous Mesoporous Mater.*, 2001, vol. 48, p. 171.
22. Fukuoka, A., Higashimoto, N., Sakamoto, Y., Sasaki, M., Sugimoto, N., Inagaki, S., Fukushima, Y., and Ichikawa, M., *Catal. Today*, 2001, vol. 66, p. 23.
23. Komarneni, S., Roy, R., and Li, Q.H., *Mater. Res. Bull.*, 1992, vol. 27, p. 1393.
24. Komarneni, S., *Ionics*, 1995, vol. 21, p. 95.
25. Laha, S.C., Kamalakar, G., and Glaser, R., *Microporous Mesoporous Mater.*, 2006, vol. 90, p. 45.
26. Jhung, S.H., Chang, J.-S., Hwang, J.S., and Park, S.-E., *Microporous Mesoporous Mater.*, 2003, vol. 64, p. 33.
27. Lohse, U., Bruckner, A., Schreier, E., Bertram, R., Janchen, J., and Fricke, R., *Microporous Mater.*, 1996, vol. 7, p. 139.
28. Tompsett, G., Conner, W.C., and Yngvesson, K.S., *Chem. Phys. Chem.*, 2006, vol. 7, p. 296.
29. Park, S.-E., Chang, J.-S., Hwang, Y.K., Kim, D.S., Jhung, S.H., and Hwang, J.-S., *Catal. Survey Asia*, 2004, vol. 8, p. 91.
30. Oberender, N. and Froba, M., *Mater. Res. Soc. Symp. Proc.*, 1999, vol. 547, p. 433.
31. Kang, K.K., Park, C.H., and Ahn, W.-S., *Catal. Lett.*, 1999, vol. 59, p. 45.
32. Newalkar, B.L., Komarneni, S., and Katsuki, H., *Chem. Commun.*, 2000, p. 2389.
33. Newalkar, B.L., Olanrewaju, J., and Komarneni, S., *Chem. Mater.*, 2001, vol. 13, p. 552.
34. Olah, G.A., *Friedel–Crafts Chemistry*, New York: Wiley, 1973.
35. Corma, A., Fornes, V., Navarro, M.T., and Perez-Pariente, J., *J. Catal.*, 1994, vol. 148, p. 569.
36. Vinu, A., Sawant, D.P., Ariga, K., Hossain, K.Z., Halligudi, S.B., Hartmann, M., and Nomura, M., *Chem. Mater.*, 2005, vol. 17, p. 5339.
37. Bachari, K., Millet, J.M.M., Benachouba, B., Cherifi, O., and Figueras, F., *J. Catal.*, 2004, vol. 221, p. 55.
38. Choudhary, V.R., Jana, S.K., and Kiran, B.P., *Catal. Lett.*, 1999, vol. 59, p. 217.
39. Choudhary, V.R. and Jana, S.K., *Appl. Catal., A*, 2002, vol. 224, p. 51.
40. Kistner, O.C. and Sunyar, A.W., *Phys. Rev. Lett.*, 1960, vol. 4, p. 412.
41. Neel, L., *Ann. Geophys.*, 1949, vol. 5, p. 99.
42. Mørup, S., Dumesic, J.A., and Topsøe, H., in *Applications of Mössbauer Spectroscopy*, Cohen, R.L., Ed., New York: Academic, 1980, vol. 2.
43. Millet, J.M.M., Knozinger, H., and Bonville, P., *J. Phys. Chem. B*, 2006, vol. 110, p. 16 003.
44. Millet, J.M.M., Signoretto, M., and Bonville, P., *Catal. Lett.*, 2000, vol. 64, p. 135.
45. Aasa, R., *J. Chem. Phys.*, 1983, vol. 52, p. 3919.
46. Golfarb, D., Bernardo, M., Strohmaier, K.G., Vaughan, D.E.W., and Thomann, H., *J. Am. Chem. Soc.*, 1994, vol. 116, p. 6344.
47. Selvam, P., Dapurkar, S.E., Badamali, S.K., Murugasan, M., and Kuwano, H., *Catal. Today*, 2001, vol. 68, p. 69.
48. Arata, K. and Oyoshima, I., *Chem. Lett.*, 1974, p. 929.
49. Arata, K., Yabe, K., and Oyoshima, I., *J. Catal.*, 1976, vol. 44, p. 385.
50. Carrier, X., Lukinskas, P., Kuba, S., Stievano, L., Wagner, F., Che, M., and Knozinger, H., *Chem. Phys. Chem.*, 2004, vol. 5, p. 1191.
51. Lin, D.H., Coudurier, G., and Vedrine, J.C., *Stud. Surf. Sci. Catal.*, 1989, vol. 49, p. 1431.
52. Bordiga, S., Buzzoni, R., Geobaldo, F., Lamberti, C., Giamello, E., Zecchnina, A., Leofanti, G., Petrini, G., Tozzola, G., and Vlaic, G., *J. Catal.*, 1996, vol. 158, p. 486.
53. Newman, M.S., *Steric Effects in Organic Chemistry*, New York: Wiley, 1956.
54. Hentit, H., Bachari, K., Ouali, M.S., Womes, M., Benaichouba, B., and Jumas, J.C., *J. Mol. Catal. A: Chem.*, 2007, vol. 275, p. 158.